

Kinetic energy transfer during polarity reversal in numerical dynamo simulation

Takumi Kera^a, Hiroaki Matsui^{b,*}, Masaki Matsushima^c, Yuto Katoh^a

^a*Department of Geophysics, Tohoku University, Sendai, Japan.*

^b*Department of the Earth and Planetary Sciences, University of California, Davis, CA, USA.*

^c*Department of Earth and Planetary Sciences, Tokyo Institute of Technology, Tokyo, Japan.*

Abstract

The Earth has a magnetic field with a dominant dipole moment nearly parallel to the axis of Earth's rotation. Paleomagnetic measurements have shown that the geomagnetic field has reversed its polarity many times. It is widely accepted that the geomagnetic field is sustained by fluid motion in the Earth's outer core, so-called dynamo action. Some geodynamo simulations have been carried out to investigate the physical process of polarity reversals, and the equatorially antisymmetric flow during reversals is found to be stronger than that during stable periods. On the other hand, convective motions in a rotating spherical shell have characteristics that the equatorially symmetric flow is dominant due to the effect of rotation. We have performed a geodynamo simulation with polarity reversals, and analyzed energy transfers between the equatorially symmetric and antisymmetric flows. The energy transfer to the equatorially antisymmetric flow is generally small, but it increases toward a polarity reversal as follows, (i) the rate of energy transfer from the equatorially symmetric flow to the magnetic field decreases, (ii) the rate of energy transfer from the equatorially symmetric flow to the antisymmetric flow by the advection increases, and (iii) the energy injection by the buoyancy force into the equatorially antisymmetric flow increases. The present results suggest that the intense zonal flow caused by the intense upward flow inside the tangent cylinder in the either hemisphere can trigger a polarity reversal of the magnetic field.

*Corresponding author

Email addresses: takumi.kera.r1@dc.tohoku.ac.jp (Takumi Kera), hrmatsui@ucdavis.edu (Hiroaki Matsui), masaki.matsushima@eps.sci.titech.ac.jp (Masaki Matsushima), yuto.katoh@tohoku.ac.jp (Yuto Katoh)

Keywords: Geodynamo, Polarity reversals, Equatorial symmetry, Energy transfer

1. Introduction

The Earth has an intrinsic magnetic field which is dominated by a dipole component roughly aligned with the Earth's rotation axis. The amplitude and direction of the past geomagnetic field can be estimated by paleomagnetic observations using igneous or sedimentary rocks. Recent paleomagnetic observations have revealed that the geomagnetic field has been sustained for 4.2 billion years (Tarduno et al., 2020). In addition, the paleomagnetic observations and observations of the magnetic anomalies around the oceanic ridges have revealed that the direction of the geomagnetic field has frequently reversed in the geological time scale (e.g. Cande and Kent, 1995). These results strongly support that the geomagnetic field is maintained by a flow motion of the liquid iron alloy in the Earth's outer core, so called the geodynamo process.

Numerical simulations of geodynamo have been playing an important role to understand the dynamo processes and magnetohydrodynamics (MHD) in the Earth's outer core. After Glatzmaier and Roberts (1995) and Kageyama et al. (1995), many MHD dynamo simulations have been successfully performed to represent the characteristics of the geomagnetic field. The polarity reversal of the axial dipole component has also been represented in the geodynamo simulations (e.g. Glatzmaier and Roberts, 1995; Sarson and Jones, 1999; Takahashi et al., 2007; Olson et al., 2011 Sreenivasan et al., 2014).

The convection in the outer core is likely to be dominated by the geostrophic balance, in which the Coriolis force is balanced by the pressure gradient. Busse (1970) suggested that the convection in a rotating spherical shell occurs mainly outside the tangent cylinder, which is an imaginary cylinder with the radius of the inner core, and that the convection is characterized by multiple convective columns along with the rotation axis. The columnar helical flow in the anti-cyclonic convection columns generates the dipolar magnetic field by twisting magnetic field lines in the anti-cyclonic columns, and the zonal magnetic field line is extended with the cyclonic convection columns (Kageyama and Sato, 2017). These convective motions in a rotating spherical shell are characterized by symmetry with respect to the equatorial plane. The Lorentz force is also nearly symmetric with respect to the equatorial plane if the magnetic

field is dominantly antisymmetric with respect to the equatorial plane such as the axial dipole field. However, it is suggested that the equatorial symmetry of the convection in the outer core is broken and equatorially symmetric components of the magnetic field increases during the polarity reversals both from the paleomagnetic observations and numerical simulations. Based on the paleomagnetic observations for the last 150 million years, the amplitude ratio of equatorially antisymmetric component excluding axial dipole component to the total off-axis dipole component of the geomagnetic field is inversely correlated with the reversal occurrence (Coe and Glatzmaier, 2006). Glatzmaier et al. (1999) showed that the equatorially antisymmetric components of the magnetic field are dominant when the axial dipole field is stably generated in their geodynamo simulations. The Earth-like magnetic dipole reversal is characterized by the stable dipole dominant magnetic field and spontaneous rapid reversal of the dipole component. Regarding flow motion, several numerical dynamo models with Earth-like polarity reversal represented a breakdown of the equatorial symmetry of the both meridional circulation and zonal flow during the dipole reversal (Li et al., 2002; Wicht and Olson, 2004). Wicht and Olson (2004) concluded that the reversed axisymmetric toroidal electric current (i.e. axisymmetric poloidal magnetic field) is generated near the outer boundary and tangent cylinder, which is an imaginary cylinder adjoint with the inner core boundary, by the plume with upwelling flow, and that equatorially anti-symmetric meridional circulation advects the reversed zonal current to the whole outer core during the reversals.

The control factors for the polarity reversal have also been examined so far. Glatzmaier et al. (1999) performed thermally driven dynamo simulations with changing heat flux patterns at the outer boundary of the spherical shell and found that more reversals occurs in the case of smaller heat flux at high latitude. Parameters used in the geodynamo simulations with Earth-like polarity reversal can generally be found between the dynamo regime to sustain stable intense dipolar field without reversal and that to generate weak and periodically variable dipole field with small scale magnetic field (Christensen and Aubert, 2006; Driscoll and Olson, 2009). Sreenivasan et al. (2014) performed dynamo simulations with various Rayleigh numbers and showed that occurrence of the polarity reversal increases with increase of the Rayleigh number. Olson

and Christensen (2006) showed that the generated magnetic fields change from dipole dominant field to multipolar magnetic field with increase of the Rayleigh number and Earth-like polarity reversal is represented in the cases with the Rayleigh number which is transferring from the dipolar to multipolar regime. In addition, they also pointed out that inertia can have a large role to give rise to polarity reversals by scaling between dipole field strength and local Rossby number. Nakagawa and Davies (2022) also performed dynamo simulations with reversing dipole components and concluded that the role of the inertia is not negligible, even if QG-MAC (Quasi-Geostrophic with Magnetic, Archimedean and Coriolis) dynamics balance is dominant during the polarity reversal.

Nishikawa and Kusano (2008) focused on the energy transfer in the magnetic induction equation separated into the equatorially symmetric and antisymmetric components. Nishikawa and Kusano (2008) mentioned that the direction of the energy transfer changes between stable dipole and reversals periods. The energy of the equatorially symmetric components of the magnetic energy transfers to the equatorially antisymmetric components of the kinetic energy during the reversals, while the energy transfers from equatorially antisymmetric kinetic energy to the equatorially symmetric components of the magnetic energy in the stable dipole period.

In the present study, we focus on how the energies of equatorially symmetric and antisymmetric flows are transferred by the buoyancy, advection, and Lorentz force. We perform MHD dynamo simulations in a rotating spherical shell modeled on the Earth's outer core and evaluate the work of the buoyancy, inertia term, and Lorentz force for the equatorially symmetric and antisymmetric components averaged over the spherical shell. In Section 2, we will explain the models of the present dynamo simulation and describe the energy equations for the equatorially symmetric and antisymmetric flows. In Section 3, we will show the results of the simulation and analyze data in terms of the work by forces. In Section 4, we will discuss the comparison with the results of previous studies and magnetic field generation processes during the polarity reversal in the present simulation. Finally, conclusions will be described in Section 5.

2. Method

2.1. Numerical method

We perform numerical simulations of a magnetohydrodynamic (MHD) dynamo to investigate mechanism related to polarity reversals of the Earth's magnetic field. The fluid outer core, in which dynamo action occurs, is represented by a spherical shell rapidly rotating with angular velocity $\Omega = \Omega \hat{z}$, where \hat{z} is the unit vector aligned to the rotation axis. The spherical shell with inner and outer radii, r_i and r_o , respectively, and $r_i/r_o = 0.35$, is filled with an electrically conducting Boussinesq fluid, which is assumed to have constant kinetic viscosity ν , thermal diffusivity κ , and magnetic diffusivity η . This leads to an equation of continuity as

$$\nabla \cdot \mathbf{u} = 0, \quad (1)$$

where \mathbf{u} is the velocity field of core fluid. The magnetic field, \mathbf{B} , satisfies the Gauss's law given as

$$\nabla \cdot \mathbf{B} = 0. \quad (2)$$

The other nondimensional governing equations for the present MHD dynamo driven by thermally convective motions are derived as

$$E \left(\frac{\partial \mathbf{u}}{\partial t} + \boldsymbol{\omega} \times \mathbf{u} \right) = -E \nabla \left(P + \frac{1}{2} \mathbf{u}^2 \right) + E \nabla^2 \mathbf{u} \\ - 2\hat{z} \times \mathbf{u} + Ra_f T \frac{\mathbf{r}}{r_o} + \frac{1}{Pm} \mathbf{J} \times \mathbf{B}, \quad (3)$$

$$\frac{\partial \mathbf{B}}{\partial t} = \nabla \times (\mathbf{u} \times \mathbf{B}) + \frac{1}{Pm} \nabla^2 \mathbf{B}, \quad (4)$$

$$\frac{\partial T}{\partial t} + (\mathbf{u} \cdot \nabla) T = \frac{1}{Pr} \nabla^2 T, \quad (5)$$

where t is the time, $\boldsymbol{\omega}$ is the vorticity, P is the pressure, \mathbf{r} is the position vector, and \mathbf{J} is the electric current density. The length, time, pressure, temperature, and magnetic field are respectively scaled by D , D^2/ν , ν^2/D^2 , $\beta_o D$, and $(\rho \mu_0 \Omega \eta)^{1/2}$, where $D = r_o - r_i$, ρ , μ_0 , and β_o are the thickness of the outer core, the mean density of the conductive fluid, the magnetic permeability of vacuum, and the temperature gradient at the core-mantle boundary (CMB), respectively. The dimensionless numbers included in the

governing equations are the Rayleigh number, Ra_f , the Ekman number, E , the Prandtl number, Pr , and the magnetic Prandtl number, Pm , which are defined as

$$Ra_f = \frac{\alpha g_o \beta_o r_o^2}{\nu \Omega}, \quad E = \frac{\nu}{\Omega D^2}, \quad Pr = \frac{\nu}{\kappa}, \quad \text{and} \quad Pm = \frac{\nu}{\eta}, \quad (6)$$

where α is the coefficient of thermal volume expansion, and g_o is the amplitude of gravity at $r = r_o$.

The solenoidal vector fields, \mathbf{u} and \mathbf{B} , are decomposed into the toroidal and poloidal components as

$$\mathbf{u}(\mathbf{r}, t) = \nabla \times (u_T(\mathbf{r}, t)\hat{\mathbf{r}}) + \nabla \times \nabla \times (u_S(\mathbf{r}, t)\hat{\mathbf{r}}), \quad (7)$$

$$\mathbf{B}(\mathbf{r}, t) = \nabla \times (B_T(\mathbf{r}, t)\hat{\mathbf{r}}) + \nabla \times \nabla \times (B_S(\mathbf{r}, t)\hat{\mathbf{r}}), \quad (8)$$

where $\hat{\mathbf{r}}$ is the radial unit vector. Toroidal and poloidal scalar functions for the velocity and magnetic fields, $u_T(\mathbf{r}, t)$, $u_S(\mathbf{r}, t)$, $B_T(\mathbf{r}, t)$, and $B_S(\mathbf{r}, t)$, are expanded into spherical harmonics in the horizontal directions. For example, $u_S(\mathbf{r}, t)$ is expanded as

$$u_S(\mathbf{r}, t) = \sum_{l=1}^{L_{\max}} \sum_{m=-l}^l u_{Sl}^m(r, t) Y_l^{|m|}(\theta, \phi), \quad (9)$$

where L_{\max} is the truncation of spherical harmonic expansion, and

$$Y_l^{|m|}(\theta, \phi) = \begin{cases} P_l^m(\cos \theta) \cos m\phi & (m = 0, 1, 2, \dots, l) \\ P_l^{|m|}(\cos \theta) \sin |m|\phi & (m = -1, -2, \dots, -l), \end{cases} \quad (10)$$

where, $P_l^m(\cos \theta)$ is a Schmidt quasi-normalized associated Legendre polynomial with degree l and order m (Winch et al., 2005). The temperature field is also expanded into the spherical harmonics coefficients as

$$T(\mathbf{r}, t) = \sum_{l=0}^{L_{\max}} \sum_{m=-l}^l T_l^m(r, t) Y_l^{|m|}(\theta, \phi). \quad (11)$$

In the radial direction, scalar functions, $u_T(\mathbf{r}, t)$, $u_S(\mathbf{r}, t)$, $B_T(\mathbf{r}, t)$, $B_S(\mathbf{r}, t)$, and $T(\mathbf{r}, t)$, are differentiated by the second-order finite difference method. To obtain high spatial resolution near the boundaries and a smooth transition of grid spacing, the so-called Chebyshev grid is used for the radial grid points defined as

$$r_n = r_i + \frac{r_o - r_i}{2} \left\{ 1 - \cos \left(\pi \frac{n-1}{N_r-1} \right) \right\} \quad (n = 1, \dots, N_r), \quad (12)$$

where N_r is the number of radial grids.

For the time integration, the Crank-Nicolson scheme is adopted for the diffusion terms, and the second order Adams-Bashforth scheme is used for the other terms.

The no-slip condition for the velocity field is imposed at impermeable boundary surfaces, and the inner core is assumed to co-rotate with the mantle, which leads to $\mathbf{u} = \mathbf{0}$. The regions outside the spherical shell corresponding to the inner core and the mantle are assumed to be electrical insulators for simplicity, so that the magnetic field in the spherical shell is continuous to a potential field both at $r = r_i$ and $r = r_o$. An uniform temperature gradient at the CMB is imposed as $-\partial T_0^0 / \partial r|_{r=r_o} = r_o^{-2} = 0.4225$. To satisfy $T_0^0(r, t)$ with $\nabla^2 T_0^0 = 0$, the temperature gradient at the inner core boundary (ICB) is determined from the balance between the heat flux into at $r = r_i$ and out from $r = r_o$. Consequently, the uniform temperature gradient at the ICB is set to $-\partial T_0^0 / \partial r|_{r=r_i} = r_i^{-2}$.

The initial condition for numerical simulations is set as follows; $\mathbf{u} = \mathbf{0}$ for the velocity field, a geocentric magnetic dipole moment whose tilt angle from the rotation axis is $\pi/4$, and a component of degree 4 and order 4 of spherical harmonics for the temperature as adopted by a dynamo benchmark (Christensen et al., 2001). The dimensionless parameters are set as $Ra_f = 2000$, $E = 6 \times 10^{-4}$, $Pr = 1$, and $Pm = 5$ on the basis of results by Sreenivasan et al. (2014).

2.2. Equatorial symmetry

We investigate possible variations in equatorial symmetry of the velocity and magnetic fields in relation to polarity reversals. Dimensionless kinetic energy density and dimensionless magnetic energy density are respectively defined as

$$E_{\text{kin}} = \frac{1}{V} \int_V \frac{1}{2} \mathbf{u}^2 dV, \quad (13)$$

$$E_{\text{mag}} = \frac{1}{VPmE} \int_V \frac{1}{2} \mathbf{B}^2 dV, \quad (14)$$

where integrals are carried out over the volume of spherical shell, V . Temporal variations of kinetic and magnetic energy densities can be derived from (3) and (4), respec-

tively. Their energy equations are given as

$$\frac{\partial}{\partial t} \int_V \frac{|\mathbf{u}|^2}{2} dV = \int_V \left\{ -|\boldsymbol{\omega}|^2 + \frac{Ra_f}{E} T \mathbf{u} \cdot \frac{\mathbf{r}}{r_o} - \mathbf{u} \cdot (\boldsymbol{\omega} \times \mathbf{u}) + \frac{1}{PmE} \mathbf{u} \cdot (\mathbf{J} \times \mathbf{B}) \right\} dV, \quad (15)$$

$$\frac{1}{PmE} \frac{\partial}{\partial t} \int_V \frac{|\mathbf{B}|^2}{2} dV = -\frac{1}{PmE} \int_V \left\{ \mathbf{u} \cdot (\mathbf{J} \times \mathbf{B}) + \frac{1}{Pm} |\mathbf{J}|^2 + \nabla \cdot (\mathbf{E} \times \mathbf{B}) \right\} dV. \quad (16)$$

Any vector can be divided into equatorially symmetric and antisymmetric constituents.

We represent the velocity and magnetic field as,

$$\mathbf{u} = \mathbf{u}^s + \mathbf{u}^a, \quad \mathbf{B} = \mathbf{B}^s + \mathbf{B}^a, \quad (17)$$

where superscripts s and a denote equatorially symmetric and antisymmetric fields, respectively. We then derive the energy equations for the equatorially symmetric and antisymmetric velocity field, respectively, given as

$$\begin{aligned} \frac{\partial}{\partial t} \int \frac{|\mathbf{u}^s|^2}{2} dV &= \int \left\{ \frac{Ra_f}{E} T^s \mathbf{u}^s \cdot \frac{\mathbf{r}}{r_o} \right. \\ &\quad \left. + \frac{1}{PmE} \mathbf{u}^s \cdot (\mathbf{J}^s \times \mathbf{B}^a + \mathbf{J}^a \times \mathbf{B}^s) \right. \\ &\quad \left. - \mathbf{u}^s \cdot (\boldsymbol{\omega}^s \times \mathbf{u}^a) - |\boldsymbol{\omega}^a|^2 \right\} dV, \end{aligned} \quad (18)$$

$$\begin{aligned} \frac{\partial}{\partial t} \int \frac{|\mathbf{u}^a|^2}{2} dV &= \int \left\{ \frac{Ra_f}{E} T^a \mathbf{u}^a \cdot \frac{\mathbf{r}}{r_o} \right. \\ &\quad \left. + \frac{1}{PmE} \mathbf{u}^a \cdot (\mathbf{J}^a \times \mathbf{B}^a + \mathbf{J}^s \times \mathbf{B}^s) \right. \\ &\quad \left. + \mathbf{u}^a \cdot (\boldsymbol{\omega}^s \times \mathbf{u}^s) - |\boldsymbol{\omega}^s|^2 \right\} dV. \end{aligned} \quad (19)$$

In the same way, the energy equations for the equatorially symmetric and antisymmetric magnetic field are respectively obtained as

$$\begin{aligned} \frac{1}{PmE} \frac{\partial}{\partial t} \int \frac{|\mathbf{B}^s|^2}{2} dV &= -\frac{1}{PmE} \int \left\{ \mathbf{u}^a \cdot (\mathbf{J}^a \times \mathbf{B}^a) + \mathbf{u}^s \cdot (\mathbf{J}^a \times \mathbf{B}^s) \right. \\ &\quad \left. + \frac{1}{Pm} |\mathbf{J}^a|^2 + \nabla \cdot (\mathbf{E}^a \times \mathbf{B}^s) \right\} dV, \end{aligned} \quad (20)$$

and

$$\begin{aligned} \frac{1}{PmE} \frac{\partial}{\partial t} \int \frac{|\mathbf{B}^a|^2}{2} dV &= -\frac{1}{PmE} \int \left\{ \mathbf{u}^a \cdot (\mathbf{J}^s \times \mathbf{B}^s) + \mathbf{u}^s \cdot (\mathbf{J}^s \times \mathbf{B}^a) \right. \\ &\quad \left. + \frac{1}{Pm} |\mathbf{J}^s|^2 + \nabla \cdot (\mathbf{E}^s \times \mathbf{B}^a) \right\} dV. \end{aligned} \quad (21)$$

The right-hand-sides of (18) and (19) show energy transfer due to respective forces as follows. The first terms corresponding to the work by buoyancy mean that equatorially symmetric and antisymmetric temperature fields contribute to kinetic energy for the equatorially symmetric and antisymmetric velocity fields, respectively. The second terms, the work by the Lorentz force, show energy transfer between kinetic and magnetic energies, as they are also found in (20) and (21); that is, $\mathbf{u}^s \cdot (\mathbf{J}^s \times \mathbf{B}^a)$ corresponds to energy transfer between \mathbf{u}^s and \mathbf{B}^a , $\mathbf{u}^s \cdot (\mathbf{J}^a \times \mathbf{B}^s)$ to that between \mathbf{u}^s and \mathbf{B}^s , $\mathbf{u}^a \cdot (\mathbf{J}^a \times \mathbf{B}^a)$ to that between \mathbf{u}^a and \mathbf{B}^a , and $\mathbf{u}^a \cdot (\mathbf{J}^s \times \mathbf{B}^s)$ to that between \mathbf{u}^a and \mathbf{B}^s . In other words, $-\mathbf{u}^s \cdot (\mathbf{J}^s \times \mathbf{B}^a)$ contributes to temporal variations of \mathbf{B}^a caused by \mathbf{u}^s , $-\mathbf{u}^s \cdot (\mathbf{J}^a \times \mathbf{B}^s)$ to those of \mathbf{B}^s by \mathbf{u}^s , $-\mathbf{u}^a \cdot (\mathbf{J}^a \times \mathbf{B}^a)$ to those of \mathbf{B}^a by \mathbf{u}^a , and $-\mathbf{u}^a \cdot (\mathbf{J}^s \times \mathbf{B}^s)$ to those of \mathbf{B}^s by \mathbf{u}^a , as found in (20) and (21). The third terms in the right-hand-sides of (18) and (19) express energy transfer between \mathbf{u}^s and \mathbf{u}^a due to the advection, which does not contribute to total kinetic energy. The fourth terms indicate the viscous dissipation. The third terms in the right-hand-sides of (20) and (21) indicate the Ohmic dissipation. The forth terms correspond to the Poynting flux which can be expressed, for example, as

$$-\int \nabla \cdot (\mathbf{E}^a \times \mathbf{B}^s) dV = \oint (\mathbf{E}^a \times \mathbf{B}^s) \cdot \hat{\mathbf{r}} dS. \quad (22)$$

We implemented subroutines to evaluate these volume averaged energy transfers decomposed to the equatorial symmetry into a numerical dynamo code, Calypso Ver. 1.2 (Matsui et al., 2014) and performed dynamo simulations with polarity reversals. The source code and documents of Calypso Ver. 1.2 can be found in the following URL;
<https://github.com/geodynamics/calypso>

3. Results

We performed a dynamo simulation with $E = 6.0 \times 10^{-4}$, $Ra_f = 2000$, $Pr = 1.0$, and $Pm = 5.0$. The dimensionless time, t , is scaled by the viscous diffusion time, $\tau_\nu = D^2/\nu$, whereas the magnetic diffusion time, $\tau_\eta = D^2/\eta = PmD^2/\nu = 5\tau_\nu$ is used to show the results of time evolution. The simulation was performed for approximately $85\tau_\eta$, and the average ratio of magnetic to kinetic energies, $E_{\text{mag}}/E_{\text{kin}}$, was approximately 0.63. The dipole tilt angle, θ_D , between the directions of rotation axis and the magnetic dipole moment was calculated from the radial component of the magnetic field with spherical harmonic degree one at the CMB.

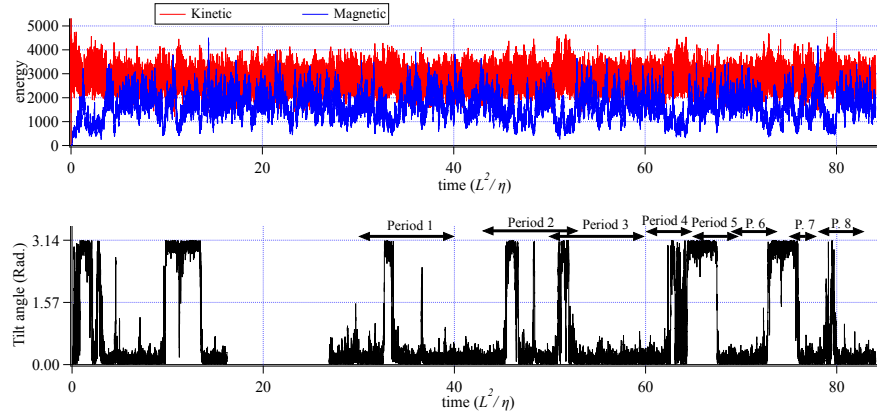


Figure 1: Time evolution of kinetic and magnetic energies (top panel) and the dipole tilt angle (bottom panel) throughout the present simulation (approximately 85 magnetic diffusion times). The dipole tilt angle between $16.2 \leq t/\tau_\eta \leq 26.9$ is not plotted due to missing of the data. After $t = 5.0\tau_\eta$, 12 polarity reversals occurred. Double headed arrows in the bottom panel show eight periods during which data analyses are carried out.

The result shows that there are periods during which the dipole field was stable and those during which 13 polarity reversals and 6 excursions occurred (see Fig. 1). In the present study, we choose 8 periods shown by double headed arrows in Fig. 1 including these polarity reversals, and investigate energy transfer among the kinetic and magnetic energies for the equatorially symmetric and antisymmetric components. We also carried out 7 simulations starting from snapshots in Period 1, 2 and 3. These results were found to depart from the original result except for the case Retry 3-2, but

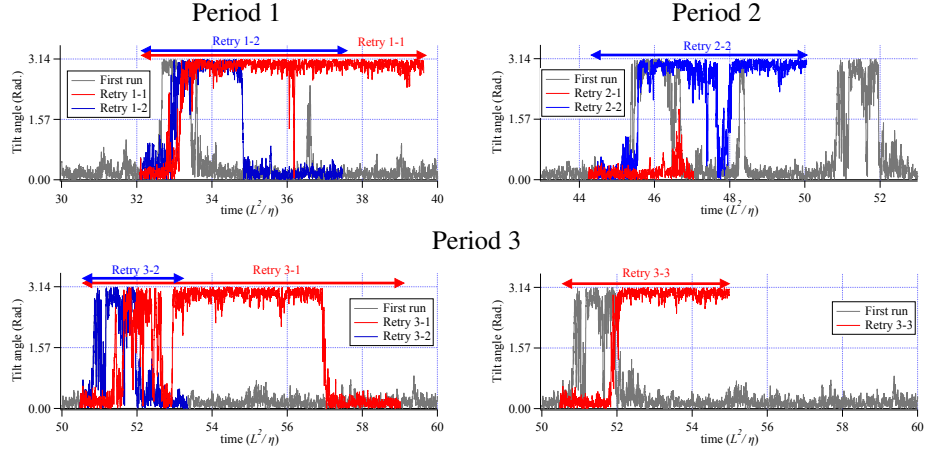


Figure 2: Time evolution of the dipole tilt angle in six retried runs. The result in the original run is plotted by gray lines. Re-calculations in Period 1 and 2 are shown in the upper left and right panels, respectively. Re-calculations in Period 3 are shown in the lower panels. Double headed arrows show periods during which data analyses are carried out.

these retried cases also include polarity reversals and excursions (see Fig. 2). We will discuss the reason why these retried cases give rise to different results in the discussion section.

3.1. Characteristics of the fields during polarity reversals

First, we investigate characteristics of the temperature field during a polarity reversal by choosing a result between $13.0 \leq t/\tau_\eta \leq 14.0$. As shown in Fig. 3b, the equatorially antisymmetric component of the temperature is larger than the equatorially symmetric component of the temperature during the polarity reversals and excursions, while the equatorially symmetric component of the temperature is approximately 1.5 times larger than the equatorially antisymmetric component. Volume rendering images of the temperature show that hot material rises strongly in the southern hemisphere during the polarity reversal, and that hot regions inside the tangent cylinder can be found in the both hemisphere before and after the reversal event (see Fig. 3 and movie in the supplement materials). However, any feature corresponding to the temperature does not appear in the radial magnetic field at the outer boundary of the spherical shell, because the upward flow along with the plumes must be diverged near the CMB and

the magnetic lines of force also diverge with the diverging flow.

Secondly, we take time averages of the fields during the stable dipole and reversing periods. We choose the amplitude of the axial dipole component given by the Gauss coefficient g_1^0 at $r = 2.8$ obtained from the poloidal magnetic field at the outer boundary of the shell, $r = r_o$. We define the reversing periods when $|g_1^0|^2 < 4.9 \times 10^{-5}$ in the present study (see Fig. 4).

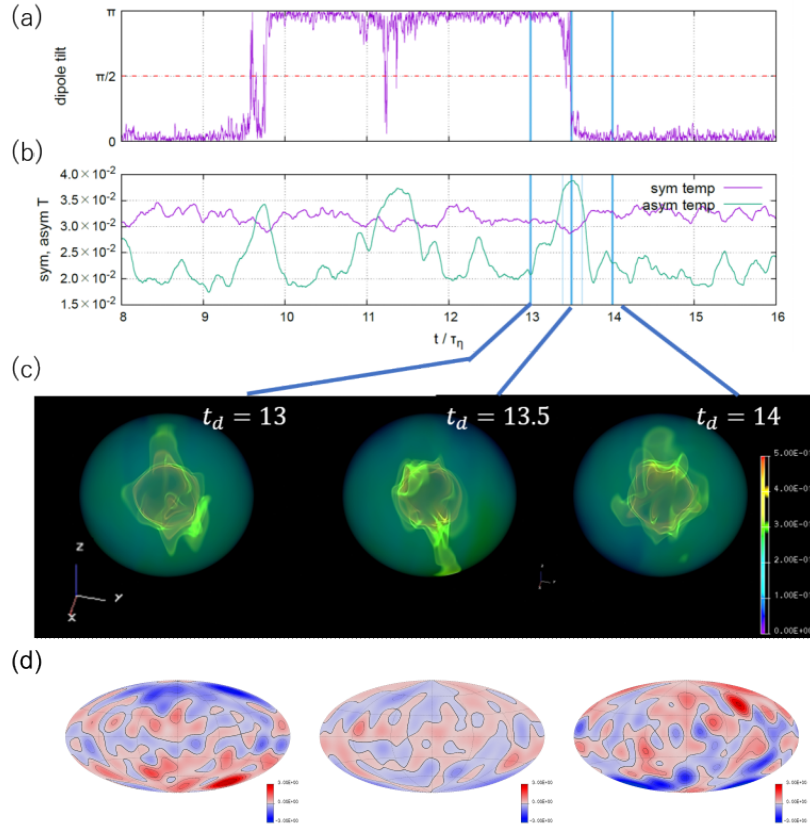


Figure 3: (a) Time evolution of the dipole tilt angle, (b) time evolution of the equatorially symmetric and antisymmetric temperature, (c) volume rendering images of the temperature, and (d) filtered radial magnetic field on the outer boundary at $t = 13.0, 13.5$ and 14.0 in the unit of the magnetic diffusion time from left to right.

Fig. 5 shows spectra of the kinetic energy and square of temperature for the equatorially symmetric and antisymmetric components with respect to the spherical harmonic order, m , for the Retry 1-1 case. We compare spectra obtained in polarity reversal peri-

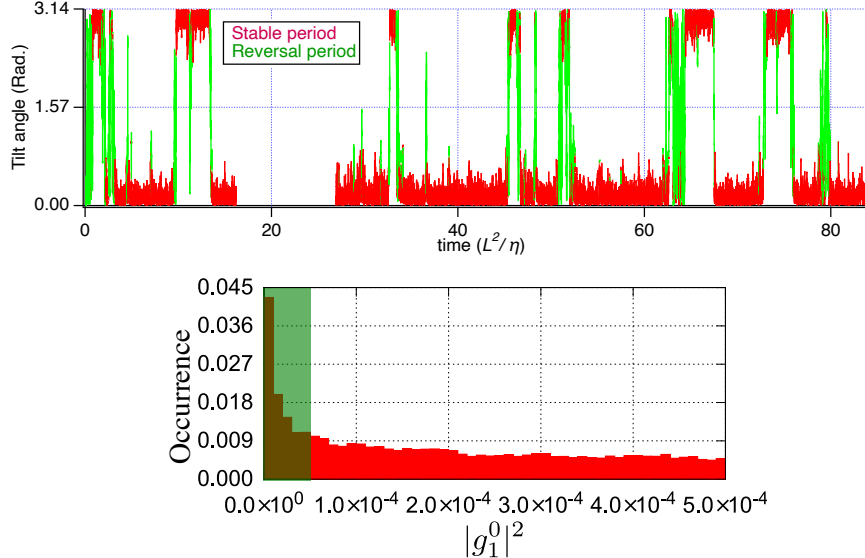


Figure 4: Time evolution of the dipole tilt angle (top panel) and histogram of the square of the Gauss coefficient $|g_1^0|^2$ with the bin size of 1.0×10^{-5} (bottom panel). The stable and reversal periods are shown by red and green dots, respectively, in the top panel. In the bottom panel, the green shaded area corresponds to the occurrence during polarity reversal periods.

ods with those in polarity stable periods. Spectra for the non-axisymmetric components ($m \neq 0$) show that the kinetic energy and square of temperature for the equatorially symmetric component are larger than those for the equatorially antisymmetric component irrespective of stable and reversal periods. Any significant difference is not found between those in stable and reversal periods, although the kinetic energy in reversal periods is slightly larger than that in stable periods.

On the other hand, amplitudes of the axisymmetric component ($m = 0$) show that the toroidal kinetic energy for the equatorially antisymmetric flow in reversal periods is approximately twice of that in stable periods, but that the toroidal kinetic energy for the equatorially symmetric flow in reversal periods is nearly equal to that in stable periods. Consequently, the toroidal kinetic energy for the equatorially antisymmetric and axisymmetric components is larger than that for the equatorially symmetric and axisymmetric components in reversal periods. It is noted that there is no remarkable

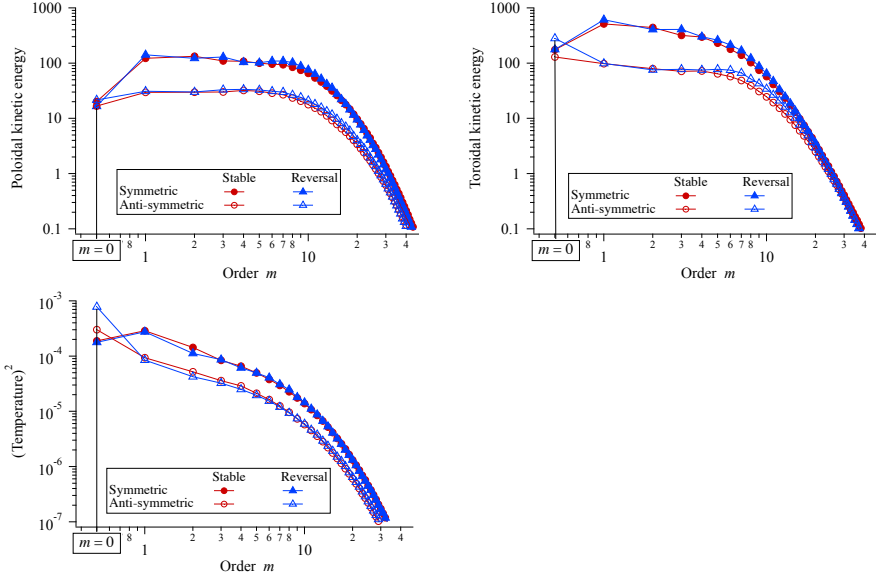


Figure 5: Spectra of poloidal kinetic energy (top left panel), toroidal kinetic energy (top right panel), and square of temperature (bottom panel) as a function of spherical harmonic order, m . The sphere averaged component T_0^0 is excluded in the temperature plot. Spectra of equatorially symmetric and antisymmetric components are plotted by filled and open symbols, respectively. Spectra in stable and reversal periods are shown by red and blue colors, respectively.

difference between poloidal kinetic energy for the equatorially symmetric and antisymmetric flows irrespective of reversal and stable periods. The spectrum of the square of the temperature has similar change as that for the toroidal kinetic energy from the stable period to the reversal period. The square of equatorially antisymmetric temperature with the axial symmetry in reversal periods is approximately three times larger than that in stable periods. A difference of the temperature spectrum from the toroidal kinetic energy spectrum is that the equatorially antisymmetric component of the axisymmetric temperature is larger than that of the non-axisymmetric temperature. Consequently, the equatorially antisymmetric temperature is larger than the equatorially symmetric temperature during reversal periods (see Fig. 3). In addition, the equatorially antisymmetric temperature with the axial symmetry is approximately 1.5 times larger than the equatorially symmetric temperature with the axial symmetry even in stable periods.

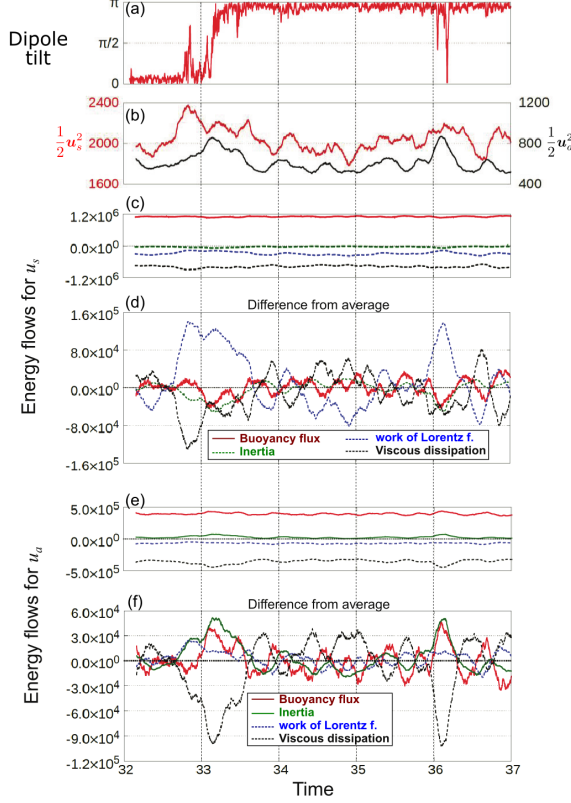


Figure 6: Time evolution of (a) the dipole tilt angle, (b) kinetic energy of the equatorially symmetric (red line) and antisymmetric (black line) components, (c) and (d) energy transfers and their deviations from their time means for the equatorially symmetric component, respectively, and (e) and (f) energy transfers and their deviations from their time means for the equatorially antisymmetric component, respectively. In (c)–(f), the buoyancy, inertial, work of Lorentz force, and viscous dissipation are plotted by red, green, blue, and black lines, respectively. Positive energy transfers (energy input) and negative ones (energy output) are plotted by solid and dashed lines, respectively.

3.2. Investigation of energy transfers

We investigate the energy transfer during polarity reversals through separation of the flow, magnetic field and temperature into the equatorially symmetric and anti-symmetric components as in eqs. (18) and (19).

First, we investigate time evolution of the energy transfers for one polarity reversal in Retry 1-1 case (see Fig. 2). Fig. 6 shows the time evolution of the dipole tilt angle, and the energy transfers between kinetic energies for the equatorially symmetric and antisymmetric flows. As described in the previous subsection, the kinetic energy for

\mathbf{u}^a does not overcome that for \mathbf{u}^s (Fig. 6b). In addition, there is no significant variation in the overall amplitude of energy transfers during the stable and reversal periods (Fig. 6c and e). Energy transfer by the buoyancy is the largest energy input to the kinetic energy for both of \mathbf{u}^s and \mathbf{u}^a . The work of Lorentz force is always negative, which means that the kinetic energy for both \mathbf{u}^s and \mathbf{u}^a is transferred to the magnetic energy. The advection always transfers energy from \mathbf{u}^s to \mathbf{u}^a (see Fig. 6c and e), although energy transfer by the advection is the smallest. Fig. 6d and f shows deviations of the energy transfers from the time average over the period for Retry 1-1, in which one polarity reversal and one excursion occurred at around $t = 33.0$ and at around $t = 36.2$, respectively (Fig. 6a). In the both events, deviation of the work by Lorentz force with the equatorial symmetry obviously increases, whereas that with the equatorial antisymmetry does not change significantly. The former corresponds to decrease of energy transfer to the magnetic field. The increase of the work by the buoyancy and advection to the equatorially antisymmetric flow is more significant than the work by Lorentz force. The work by the advection increases first, and that by the buoyancy in the next. The energy transfer by inertia increases the axisymmetric toroidal flow with the equatorial antisymmetry (see Fig. 5), because the buoyancy can be only the energy input to the poloidal flow.

Next, we investigate the energy transfer to the kinetic energy for the 11 periods in total including the stable and reversal periods (see Figs. 1 and 2). We took time averages of the work by the Lorentz force, advection, and buoyancy to the equatorially symmetric and anti-symmetric flows in reversal periods, and calculated their deviations from the time averages. The deviation of the work by Lorentz force and advection is similar to each other in the all periods, while the deviation of the work by buoyance shows large variability among the periods (see Fig. 7). The energy transfer from the equatorially symmetric flow to the magnetic field decreases (i.e. the deviation of the work by Lorentz force increases). The energy transfer to \mathbf{u}^a by the work of Lorentz force also decreases, although its amplitude is small. The largest change is found in the energy transfer from \mathbf{u}^s to \mathbf{u}^a due to the work by advection. The work by buoyancy caused by equatorially antisymmetric temperature T^a also increases in most of the cases, although its amplitude is smaller than that by the advection. The temperature

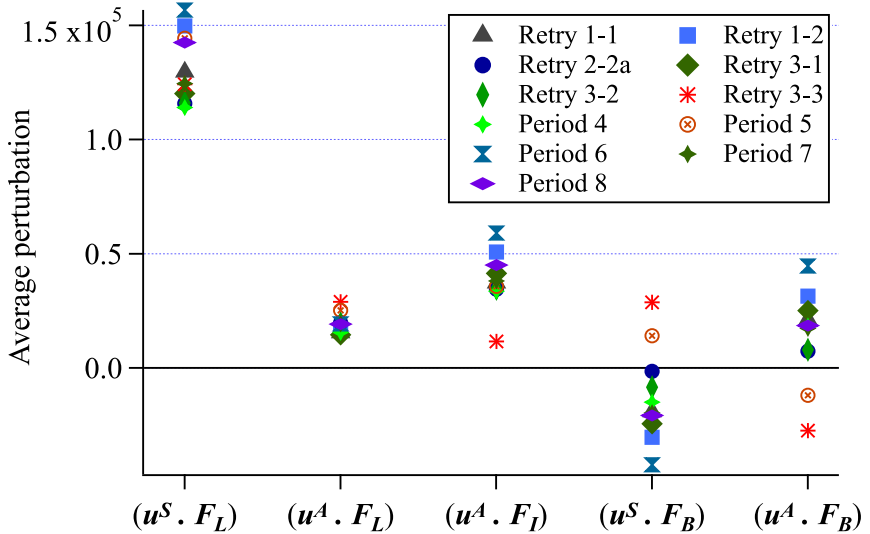


Figure 7: Time and volume average of difference of energy transfers in reversal periods from those in the stable period for calculations in Period 4 to 8 and re-calculations in the Period 1 to 3. $(\mathbf{u}^s \cdot \mathbf{F}_L)$ and $(\mathbf{u}^a \cdot \mathbf{F}_L)$ indicate energy fluxes into equatorially symmetric and antisymmetric components by Lorentz force $(PmE)^{-1} \mathbf{u}^s \cdot (\mathbf{J} \times \mathbf{B})$ and $(PmE)^{-1} \mathbf{u}^a \cdot (\mathbf{J} \times \mathbf{B})$, respectively. $(\mathbf{u}^a \cdot \mathbf{F}_I)$ is the energy flux to equatorially antisymmetric components by advection term $-\mathbf{u}^a \cdot (\boldsymbol{\omega} \times \mathbf{u})$. $(\mathbf{u}^s \cdot \mathbf{F}_B)$ and $(\mathbf{u}^a \cdot \mathbf{F}_B)$ indicate buoyancy flux for the equatorially symmetric and antisymmetric components $RaE^{-1} \mathbf{u}^s \cdot \mathbf{rT}$ and $RaE^{-1} \mathbf{u}^a \cdot \mathbf{rT}$, respectively.

structure during the reversal in Fig. 3 and change of the kinetic energy spectra in Fig. 5 suggest that the intense equatorially antisymmetric flow with the axial symmetry is induced by the advection to sustain the thermal wind inside the tangent cylinder.

Taking into account the time evolution of the energy transfer in Fig. 6, we can summarize the process of the polarity reversal as shown in Fig. 8. First, the energy transfer to the magnetic energy decreases. Secondly, the advection transfers energy from the equatorially symmetric flow to the axisymmetric zonal flow inside the tangent cylinder in the either hemisphere to sustain the thermal wind balance. Finally, the buoyancy inside the tangent cylinder drives upwelling flow and enhances the equatorially anti-symmetric temperature.

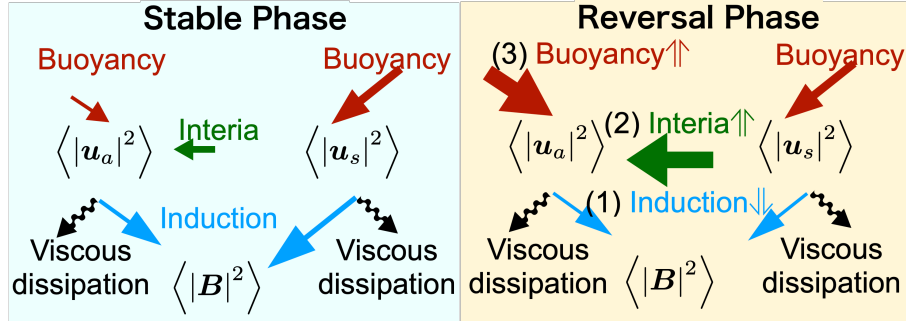


Figure 8: Schematic diagram of energy transfer for the equatorially symmetric and antisymmetric components of kinetic energy. The energy transfer in the stable dipole phase is shown in the left, and the change of the energy transfer in the reversal phase is shown in the right.

4. Discussion

We restarted numerical simulations a few times from the identical snapshot using the same dimensionless numbers and the time step Δt . However, we obtained results different from the original one; the solutions are not exactly identical as found in the evolution of the dipole tilt angle after a few magnetic diffusion time (see Fig. 2). Calypso chooses the fastest algorithms for the Legendre and Fourier transforms at the initialization process in numerical simulations. The different order of summation can change the last digit of data. As a result, numerical errors accumulate with the time integration. We found, however, that polarity reversals occur in the same way, and that the statistical results are similar to the original one. Hence, we consider that the present results are substantial and feasible.

The dimensionless numbers adopted in the present study are based on those used by Sreenivasan et al. (2014). As shown in Fig. 9, however, we obtained a solution of multipolar dominated dynamo for $Ra_f = 2700$, although Sreenivasan et al. (2014) obtained Earth-like dipole reversals with the same Rayleigh number (it is noted that Sreenivasan et al. (2014) defined the Rayleigh number as $Ra_f = \alpha g_o \beta_o D^2 / 2\Omega\nu$). The difference is likely to originate from the different thermal boundary condition at the inner boundary. We fixed the heat flux at the inner boundary, while Sreenivasan et al. (2014) fixed the temperature at the inner boundary. The uniformly fixed temperature

boundary condition forces the temperature to be equatorially symmetric at the inner boundary, although the temperature can be equatorially antisymmetric away from the inner boundary. Consequently, Sreenivasan et al. (2014) required a larger Rayleigh number to give rise to the equatorially antisymmetric temperature and flow in turn. However, no polarity reversal can be found in the cases of $Ra_f = 1500$ in the present study and $Ra_f = 1620$ in Sreenivasan et al. (2014) (See left panel of Fig. 9). The result suggests that the thermal boundary condition at the ICB does not have a significant effect on the lower bound of Ra_f to give rise to the polarity reversal.

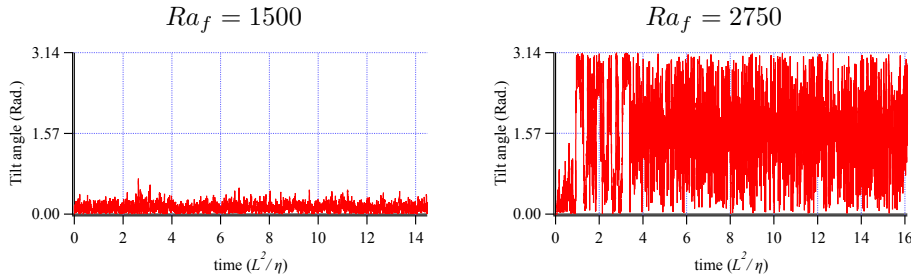


Figure 9: Time evolution of dipole tilt angle for $Ra_f = 1500$ (left panel) and $Ra_f = 2750$ (right panel).

Nishikawa and Kusano (2008) investigated energy transfers to \mathbf{B}^s and \mathbf{B}^a by \mathbf{u}^s and \mathbf{u}^a and the magnetic diffusion in the induction equation. They concluded that the magnetic induction by \mathbf{u}^a increases during polarity reversals. It should be noted that Nishikawa and Kusano (2008) adopted compressibility of core fluid and that the magnetic boundary condition and dimensionless numbers are different from those in the present dynamo model. Especially, Nishikawa and Kusano (2008) adopted larger magnetic Prandtl numbers ($Pm = 10 \sim 15$). The role of the Lorentz force increases with the magnetic Prandtl number Pm in the dynamics of the fluid motion. The difference of the magnetic Prandtl number can change the most important term for the polarity reversal process.

In the present study, we mainly investigate the dynamics and energetics of the flow during polarity reversals. Now, we discuss the process of the magnetic field generation during polarity reversals. At the beginning of a reversal process, the amplitude of the

dipole component decreases with decreasing the energy transfer from \mathbf{u}^s by the Lorentz force. When the kinetic energy for \mathbf{u}^a increases by the advection and buoyancy, the axial dipole component decreases and intense radial magnetic field is generated around the warm upward flow near the tangent cylinder in the either hemisphere. The upward flow also goes out of the tangent cylinder and reaches near the CMB in low latitude. At the end of the reversal, the warm upward flow comes out of the tangent cylinder. The flow can intensify the convection columns which generate the magnetic field. Consequently, the dipolar magnetic field with the opposite polarity increases in the outside of tangent cylinder with decreasing the equatorially antisymmetric flow and temperature.

The result in the present study is consistent with a process of polarity reversal proposed by Wicht and Olson (2004), although it indicates that the strong hot plume is generated in either one hemisphere during polarity reversals. Another difference from the results by Wicht and Olson (2004) is that the intense magnetic field generated inside the tangent cylinder changes its direction frequently during the polarity reversal. The intense equatorially antisymmetric zonal flow can generate intense equatorially symmetric zonal toroidal magnetic field with satisfying the thermal wind balance, and then columnar convective flow can generate the poloidal magnetic field with opposite polarity from the original dipolar field. The poloidal magnetic field is likely to be induced by conversing and upward flow motion along with the plumes from the bottom of the outer core. This polodal magnetic field is not axisymmetric when the plume goes to the outside of the tangent cylinder. Consequently, the generated field expands to global spherical shell (i.e. axisymmetric) to construct the reversed dipolar magnetic field. We focus on the global energy transfer in the present study. Investigations of detailed reversal processes are required as a future study.

We conclude that increase of the equatorially antisymmetric flow with the axial symmetry is the primary cause of the polarity reversal in the present geodynamo model. However, it is still difficult to evaluate how much equatorially antisymmetric flow is required to initiate a reversal or an excursion quantitatively. We need more examples of polarity reversals to investigate statistically, and we also need more simulations with dipolar dominant field and polarity reversals for different parameters, especially lower Ekman and magnetic Prandtl numbers. To perform numerical simulations with a much

smaller Ekman number, much higher spatial resolution or some sub-grid scale (SGS) model is required. Aubert (2019) pointed out that the hyperdiffusivity is feasible to model a turbulence process for the geodynamo modeling, because the role of turbulence is much smaller to the fluid dynamics in the core. However, the present study suggests that the inertia term can play an important role to drive the equatorially antisymmetric flow with axial symmetry during polarity reversals. We need further investigation to clarify which length scales of flow are important to generate the equatorially antisymmetric flow with axial symmetry and whether or not a more sophisticated model is required to represent the process to control this flow component.

5. Conclusions

We performed numerical simulations of dynamo in a rotating spherical shell for approximately 90 magnetic diffusion times and obtained 12 reversals and 4 excursions to understand the process of the polarity reversal of the magnetic field. We investigated the energy transfer for the convection during polarity reversals with special emphasis on symmetry with respect to the equatorial plane.

First, we examined the characteristics of the temperature field during one polarity reversal. We found that the equatorially antisymmetric temperature becomes larger than the equatorially symmetric one, and that the intense upward flow is generated inside the tangent cylinder in the southern hemisphere. Next, we examined the spectra of the kinetic energy and square of temperature as a function of the spherical harmonic order, m , during polarity reversals. The equatorially antisymmetric toroidal flow and temperature with the axial symmetry are found to increase significantly during polarity reversals. These results suggest that the equatorially antisymmetric zonal toroidal flow is generated to sustain the thermal wind balance around the hot upwelling flow in the tangent cylinder.

The energy transfer during the polarity reversal changes in the following way: (i) the energy transfer from the kinetic energy for the equatorially symmetric flow by the Lorentz force decreases, (ii) the energy transfer from the equatorially symmetric to antisymmetric kinetic energies increases, and (iii) the energy transfer to the kinetic energy for the equatorially antisymmetric flow by the buoyancy increases. The change

of the energy transfer to/from the kinetic energy for the equatorially antisymmetric flow indicates that the work by inertia is the largest, and the buoyancy follows it. These results are common among the 10 of 11 periods during which polarity reversals and excursions occurred. The change of the kinetic energy during the polarity reversal shows that the work by the inertia contributes to increase of kinetic energy for the equatorially antisymmetric flows with the axial symmetry around the tangent cylinder. These results suggest that the intense zonal flow caused by the intense upward flow inside the tangent cylinder in the either hemisphere can trigger a polarity reversal of the magnetic field.

Acknowledgments

The present study is supported by NSF EAR-1550901 (Computational Infrastructure for Geodynamics). This study used the computational resources of the HPCI system provided by the Research Institute for Information Technology, Kyushu University through the HPCI System Research Project (Project IDs: hp210022 and hp220040), the Polar Science Computer System in the Communications and Computing science Center (CCC) of the National Institute of Polar Research (NIPR), and Frontera High Performance Computing resource in the Texas Advanced Computing Center (TACC).

References

- Aubert, J., 2019. Approaching Earth’s core conditions in high-resolution geodynamo simulations. *Geophys. J. Int.* 219 (Supplement 1), S137–S151. <https://doi.org/10.1093/gji/ggz232>.
- Busse, F.H., 1970. Thermal instabilities in rapidly rotating systems. *J. Fluid Mech.* 44(3), 441–460.
- Cande, S.C., Kent, D.V., 1995. Revised calibration of the geomagnetic polarity timescale for the Late Cretaceous and Cenozoic. *J. Geophys. Res.* 100 (B4), 6093–6095. <https://doi.org/10.1029/94JB03098>.
- Christensen, U.R., Aubert, J., 2006. Scaling properties of convection-driven dynamos in rotating spherical shells and application to planetary fields. *Geophys. J. Int.* 166, 97–114.

- Coe, R.S., Glatzmaier, G.A., 2006. Symmetry and stability of the geomagnetic field. *Geophys. Res. Lett.* 33(21), doi:10.1029/2006GL027903.
- Driscoll, P., Olson, P., 2009. Effects of buoyancy and rotation on the polarity reversal frequency of gravitationally driven numerical dynamos. *Geophys. J. Int.* 178 (3), 1337–1350. <https://doi.org/10.1111/j.1365-246X.2009.04234.x>.
- Glatzmaier, G.A., Coe, R.S., Hongre, L., Roberts, P.H., 1999. The role of the Earth's mantle in controlling the frequency of geomagnetic reversals. *Nature* 401(6756), 885–890.
- Glatzmaier, G.A., Roberts, P.H., 1995. A three-dimensional self-consistent computer simulation of a geomagnetic field reversal. *Nature* 377(6546), 203–209.
- Kageyama, A., Sato, T., 1997. Generation mechanism of a dipole field by a magnetohydrodynamic dynamo. *Phys. Rev. E* 55(4), 4617–4626.
- Kageyama, A., Sato, T., the Complexity Simulation Group, 1995. Computer simulation of a magnetohydrodynamic dynamo, II. *Phys. Plasmas* 2(5), 1421–1431.
- Li, J., Sato, T., Kageyama, A., 2002. Repeated and sudden reversals of the dipole field generated by a spherical dynamo action. *Science* 295(5561), 1887–1890.
- Matsui, H., King, E., Buffett, B., 2014. Multiscale convection in a geodynamo simulation with uniform heat flux along the outer boundary. *Geochem. Geophys. Geosys.* 15(8), 3212–3225. <https://doi.org/10.1002/2014GC005432>.
- Nakagawa, T., Davies, C.J., 2022. Combined dynamical and morphological characterisation of geodynamo simulations. *Earth Planet. Sci. Lett.* 594, 117752. <https://doi.org/10.1016/j.epsl.2022.117752>.
- Nishikawa, N., Kusano, K., 2008. Simulation study of the symmetry-breaking instability and the dipole field reversal in a rotating spherical shell dynamo. *Phys. Plasmas* 15(8), 082903.
- Olson, P., Christensen, U.R., 2011. Dipole moment scaling for convection-driven planetary dynamos. *Earth Planet. Sci. Lett.* 250, 561–571.
- Olson, P.L., Glatzmaier, G.A., Coe, R.S., 2011. Complex polarity reversals in a geodynamo model. *Earth Planet. Sci. Lett.* 304(1)–(2), 168–179, doi:10.1016/j.epsl.2011.01.031.
- Sarson, G., Jones, C., 1999. A convection driven geodynamo reversal model. *Phys.*

Earth Planet. Inter. 111, 3–20.

- Sreenivasan, B., Sahoo, S., Dhama, G., 2014. The role of buoyancy in polarity reversals of the geodynamo. *Geophys. J. Int.* 199(3), 1698–1709.
- Takahashi, F., Matsushima, M., Honkura, Y., 2007. A numerical study on mangnetic polarity transition in an MHD dynamo model. *Earth Planets Space* 59(7), 665–673.
- Tarduno, J.A., Cottrell, R.D., Bono, R.K., Oda, H., Davis, W.J., Fayek, M., van't Erve, O., Nimmo, F., Huang, W., Thern, E.R., Fearn, S., Mitra, G., Smirnov, A.V., Blackman, E.G., 2020. Paleomagnetism indicates that primary magnetite in zircon records a strong Hadean geodynamo. *Proc. Nat. Acad. Sci.* 117(5), 2309.
- Wicht, J., Olson, P., 2004. A detailed study of the polarity reversal mechanism in a numerical dynamo model: reversal mechanism. *Geochem. Geophys. Geosys.* 5 (3), doi:10.1029/2003GC000602.
- Winch, D.E., Ivers, D.J., Turner, J.P.R., Stening, R. J., 2005. Geomagnetism and Schmidt quasi-normalization. *Geophys. J. Int.* 160 (2), 487–504.